Two types of helical core equilibrium states in tokamak plasmas

S. Kawagoe, A. Ishizawa, N. Aiba*, and Y. Nakamura

Graduate School of Energy Science,

Kyoto University, Uji, Kyoto, 611-0011, Japan. and

**National Institutes for Quantum Science and Technology, Naka, Ibaraki, 311-0192, Japan.*

(Dated: June 28, 2022)

Abstract

Helical distortion in the core region and its formation mechanism in weakly reversed magnetic shear tokamak plasmas are investigated by means of three-dimensional magnetohydrodynamic (MHD) equilibrium calculations and an MHD stability analysis. It is found that there are two different types of helical equilibrium states: one is a rigid-body shift in the core region on a poloidal cross-section, while the other is a local advection only around the magnetic axis. Linear stability analysis of the corresponding axisymmetric equilibrium is carried out for understanding the origin of these two types of helical equilibrium states. The analysis shows that the former is related to the current-driven internal kink instability, while the latter is linked to the pressure-driven quasi-interchange instability. The kink-mode driven helical equilibrium state appears when the minimum value of the safety factor q_{min} is close to unity, while the quasi-interchange driven helical equilibrium state appears when q_{min} is below unity. The appearance of the quasi-interchange state is attributed to the weak magnetic shear at the inner $q = 1$ rational surface and finite β.

I. INTRODUCTION

Non-axisymmetric equilibrium states of tokamak plasmas characterized by a helical distortion in the core region are known as helical cores, and could harm confinement of fusion plasmas such as the enhancement of fast-particle losses [1]. These non-axisymmetric equilibrium states attract attention because they are observed in tokamak discharges testing the ITER hybrid scenario that has weakly reversed magnetic shear magnetic configuration [2–4] and is expected to be favorable for reducing turbulent transport, for instance, having better β dependence of turbulent transport [5]. Helical cores are observed in JET[6], MAST[7], NSTX [1], DIII-D [8], and JT-60U [9] and are sustained long time by keeping the minimum value of the safety factor q around unity, and accordingly the helical deformation has $m = 1$ period in the poloidal direction and $n = 1$ period in the toroidal direction.

Theoretical analysis revealed that helical cores are bifurcated magnetohydrodynamic (MHD) equilibrium states [10, 11]. For an axisymmetric boundary condition on the plasma surface, we have two MHD equilibrium states: an axisymmetric equilibrium and a non-axisymmetric one with a helical distortion in the core region, which is similar to a saturated state of an internal kink-mode [11]. The conditions for the appearance of the bifurcated equilibrium are extensively studied by theoretical and numerical means. Helical cores appear when the q-profile is flat or weakly reversed in the core region, the minimum value of q is close to unity $q_{\rm min} \approx 1$, and the value of q at the plasma surface is lower than four [12–15]. In addition, there is a critical onset normalized pressure β value for the formation of a helical core [11], and the onset is also sensitive to the magnetic shear, accordingly the helical distortion increases with increasing the radial location of $q_{\rm min}$ for weakly reversed shear configurations [16]. The $q_{\rm min}$ scan shows that the maximum distortion is at a $q_{\rm min}$ of around unity [1, 11, 12, 15], although a helical core appears at a $q_{\rm min}$ of above unity. Recently, it is found that the plasma boundary shape influences the amplitude of the helical distortion, for instance, the triangularity enhances the helical distortion and lowers the critical onset β value for the formation of a helical core [17]. It is also found that such a shaped tokamak can exhibit another bifurcated equilibrium state due to external kink/peeling modes [18]. In addition, reversed D-shape plasmas are also found to exhibit a helical core [17].

The development of a helical core is related to the linear stability of $(m, n) = (1, 1)$ internal-kink modes [19–21], so that the magnetic shear at $q = 1$ surface suppresses the

formation, while the pressure gradient enhances it [16, 21, 22, 24–26]. The enhancement of the distortion by increasing the triangularity [17] is consistent with the shape dependence of the linear stability of internal-kink modes [21, 25]. A direct link between a helical equilibrium state and linear stabilities is demonstrated by nonlinear MHD simulations [23, 24]. The simulations show that the linear growth of an ideal internal-kink mode gets saturated in its nonlinear development, and then a helical equilibrium state is established. As a result, the amplitude of the helical distortion in the equilibrium state is related to the linear growth rate of the internal-kink instability of the corresponding axisymmetric equilibrium [26].

In this paper, we present two different types of equilibrium states with a helical core depending on the minimum value of reversed-shear safety factor $q_{\min}$ by means of three-dimensional MHD equilibrium calculations and a linear stability analysis of the corresponding axisymmetric equilibrium. At a $q_{\min}$ of around unity, a helical core is driven by an internal-kink instability and exhibits a rigid-body displacement in the core region. On the other hand, at a $q_{\min}$ of below unity, a helical core is generated by a quasi-interchange instability which causes a local advection of the magnetic axis. We also found that the presence of quasi-interchange driven helical cores is due to a weak magnetic shear at the inner $q = 1$ rational surface. Since the radial profiles of these instabilities are different, the resulting helical equilibrium states exhibit significantly different helical-distortion profiles on a poloidal cross section.

The organization of the remainder of this paper is as follows. Section II describes our numerical method. We present two types helical equilibrium states: internal-kink and quasi-interchange driven states in Sec. III, then we investigate the excitation mechanism of these two types in Sec. IV. The magnetic shear dependence of the quasi-interchange driven helical-core is described in Sec. V. We summarize our results in Sec. VI.

II. NUMERICAL METHOD

In order to calculate a three-dimensional MHD equilibrium for given q and pressure profiles, we use the VMEC code [27–29]. We also calculate an axisymmetric MHD equilibrium which has the same q and pressure profiles as the helical equilibrium state, using the MEUDAS code [30] that solves the Grad-Shafranov equation. Then, we calculate the linear MHD stability of the axisymmetric equilibrium by using the MINERVA code [31] to understand

the formation mechanism of the helical equilibrium state.

We investigate the helical-core formation in weakly reversed magnetic shear plasmas. First, we calculate an axisymmetric equilibrium by using the MEUDAS code for given toroidal current and pressure profiles $J_t = (1-\psi_p^b)^c + \alpha \exp[(\psi_p - \psi_0)^2/(2\sigma)]$ and $p = 1 - \psi_p$ as a function of the poloidal flux ψ_p, where $b = 4$, $c = 10$, $\alpha = 1$, $\sigma = 0.2$, and $\psi_0 = 0.53$ with the total current 1 [MA]. The corresponding safety factor profile q is weakly reversed in the core region as shown in Fig. 1. In order to decrease the minimum value of the safety factor $q_{\rm min}$, we reduce the strength of the toroidal magnetic field in our calculations. The major and minor radii are $R_0 = 3\ m$ and $a = 1\ m$, respectively. The normalized plasma pressure is defined by the volume averaged toroidal beta $\beta \equiv \beta_t = 2\mu_0 \int pdV/(VB_t^2)$, where V is the plasma volume. We calculate MHD equilibria for various shapes of the last-closed magnetic surface by varying the elongation and triangularity from $(\kappa, \delta) = (1, 0)$ to (1.8,0.344).

Three-dimensional MHD equilibrium states are calculated by using the VMEC code [27–29] which minimizes the plasma potential energy by means of the steepest-decent method. The inputs for the VMEC code are the profiles of the rotational transform $\iota(s) = \sum_{n=0}^{6} l_n s^n = 1/q(s)$ and pressure $p(s) = p_0 \sum_{n=0}^{5} p_n s^n$ obtained by interpolating the output from the MEUDAS code with the method of least squares, where the normalized toroidal flux is given by the poloidal flux as $s = \int_0^{\psi_t} q(\psi_p)d\psi_p / \int_0^1 q(\psi_p)d\psi_p$. We impose a fixed boundary condition that has up-down symmetry, and the boundary shape of the plasma is represented in terms of the ellipticity κ, triangularity δ, and aspect ratio $A = 3$ as described in Ref. [17]. In order to obtain helical cores in low $q_{\rm min}$ regime, we need to increase the number of radial grid points from $N_s = 251$ to $N_s = 3001$ as discussed in Ref. [17]. We use eight modes for toroidal and poloidal spectrum, i.e. $-8 \le n_{\rm tor} \le 8$ and $0 \le m_{\rm pol} \le 8$, in most of our calculations. We increased the number of modes up to 20 and confirmed the convergence. We do not use the GMRES preconditioning [14] in most of our calculations, but we confirmed that the GMRES preconditioning does not influence the converged states presented in this work. We define the amplitude of the helical distortion of the magnetic axis by the transverse displacement of the axis $R_{01}^{\rm ax} \equiv R_{01}(s = 0, \theta, \zeta)$, and use the normalized displacement $\delta_H \equiv R_{01}^{\rm ax}/a$ in figures, where a is the plasma minor radius. It is noted that our definition of the helical displacement is simplified from $\sqrt{(R_{01}^{\rm ax})^2 + (Z_{01}^{\rm ax})^2}/a$ used in other work[12, 14]. We omit $Z_{01}^{\rm ax}$ to avoid some inconvenience in the comparison of δ_H for different elongation values, because $Z_{01}^{\rm ax}$ becomes large for large elongations when we normalize δ_H by the minor radius.

The stability of the axisymmetric equilibrium obtained from the MEUDAS code [30] is evaluated by using the MINERVA code [31] which calculates the linear growth rate of instabilities and associated eigen-functions based on the energy principle of ideal MHD by using the eigen-value method.

III. TWO TYPES OF HELICAL CORES

First, we describe the outlook of two types of helical cores observed in our three-dimensional MHD equilibrium calculations. Figure 2 shows magnetic flux surfaces at a toroidal angle $\phi = 0$ for $\kappa = 1.2$, $\delta = 0$, and $\beta = 3\%$. For $q_{\rm min} \geq 0.86$, we obtain a helical-core structure of the flux surfaces that exhibit a rigid-body displacement in the core region inside the $q = 1$ surface. This type of helical-core is similar to the plasma displacement in the core region due to an $(m, n) = (1, 1)$ internal kink mode, and is commonly observed in our previous work [17]. For $q_{\rm min} = 0.80$, by contrast, the contours are significantly squeezed in the core region, and the magnetic axis is locally advected to the outer-board of the torus. This deformed helical-core is significantly different from the internal-kink type observed at $q_{\rm min} \geq 0.86$, and it will turn out to be caused by a quasi-interchange mode as presented below. These features do not depend on the shapes of the cross-section as shown by magnetic surfaces for $\kappa = 1.6$, $\delta = 0.344$ in Fig. 3. It is remarked that a large number of grid points is required in radial direction to obtain the quasi-interchange type helical-core in calculations using the VMEC code, specifically, we set the number of radial grid points up to $N_s = 3001$ in our calculations.

These two types of helical cores are formed in different $q_{\rm min}$ regimes. Figure 4 shows the helical displacement δ_H as a function of the minimum value of the safety factor $q_{\rm min}$ for several shapes of the cross-section characterized by the elongation and triangularity (κ, δ). There are two peaks for each shape of the plasma surface, which correspond to the two types of helical cores, except for the circular cross-section $(\kappa, \delta) = (1, 0)$. At a $q_{\rm min}$ of around unity, we have a peak of the displacement δ_H corresponding to the internal-kink driven helical-core which has a larger displacement for a larger shaping (κ, δ). On the other hand, at a $q_{\rm min}$ of about 0.8, we have another peak corresponding to the quasi-interchange driven helical-core. It is remarked that the amplitude of the peak is not so influenced by the shaping for this type of helical-core.

IV. MECHANISM OF THE APPEARANCE OF TWO TYPES

In this section, we will investigate the formation mechanism of the helical equilibrium states observed in the previous section by means of linear stability analysis of the corresponding axisymmetric equilibrium. The stability is evaluated by using the MINERVA code [31]. We calculate an axisymmetric equilibrium that has the same q and pressure profiles as the helical-core equilibrium by using the MEUDAS code [30], then we calculate the linear stability of this axisymmetric equilibrium by using the MINERVA code.

Here, we compare the helical displacement δ_H and the linear growth rate γ of an $(m, n) = (1, 1)$ instability of the corresponding axisymmetric equilibrium. Figure 5 shows the helical displacement δ_H and linear growth rate γ as a function of $q_{\rm min}$ for the cases of $(\kappa, \delta) = (1.6, 0.344)$ and $(1.8, 0.344)$. The finite δ_H and positive γ span the same $q_{\rm min}$ regime, and thus the helical core can be a nonlinearly saturated state of an $(m, n) = (1, 1)$ MHD instability. Both of the helical displacement and growth rate have their peaks at a $q_{\rm min}$ of about unity. The peak of the growth rate is caused by the current-driven internal-kink mode because the pressure driven term is very small compared to the current driven term in the ideal MHD energy principle [34] as shown in Fig. 6. Figure 6 shows the ratio of the pressure driven term $\delta W_{\rm pre}$ to the current driven term $\delta W_{\rm cur}$ as a function of $q_{\rm min}$ for $(\kappa, \delta) = (1.8, 0.344)$ at $\beta = 3\%$. The ratio $\delta W_{\rm pre}/\delta W_{\rm cur}$ is very small at $0.9 < q_{\rm min} < 1$, implying that the instability in this regime is a current-driven internal-kink mode. Thus, the helical core is driven by a current-driven internal-kink mode when the $q_{\rm min}$ is close to unity.

Next, we investigate the mechanism of the helical core formation in the low $q_{\rm min}$ regime, $q_{\rm min} \approx 0.8$. Figure 5 shows a shoulder of the linear growth rate at a $q_{\rm min}$ of around 0.8 where the helical displacement has a sharp peak. This shoulder of the growth rate suggests that there is another instability causing the helical core at a $q_{\rm min}$ of around 0.8. When the shoulder appears at $q_{\rm min} < 0.85$ in Fig. 5, the ratio $\delta W_{\rm pre}/\delta W_{\rm cur}$ in Fig. 6 correspondingly becomes finite at $q_{\rm min} < 0.85$, and thus the pressure term play a role in destabilizing the $(m, n) = (1, 1)$ mode at $q_{\rm min} < 0.85$. The pressure driven term $\delta W_{\rm pre}$ becomes comparable to the current driven term $\delta W_{\rm cur}$ at $q_{\rm min} = 0.82$, and then dominates the drive of instability at $q_{\rm min} = 0.77$, implying that the shoulder of the growth rate of $(m, n) = (1, 1)$ mode is caused by a pressure-driven quasi-interchange mode. Hence, the helical state in the low $q_{\rm min}$ regime is driven by a pressure-driven quasi-interchange mode. The transition from the internal-kink

mode to the quasi-interchange mode is continuous as $\delta W_{\rm pre}/\delta W_{\rm cur}$ increases gradually with decreasing $q_{\rm min}$.

In addition to the driving mechanism of instabilities, the plasma displacement of the instability suggests that the instabilities at $q_{\rm min} \approx 1$ and 0.8 are significantly different. The peak of the growth rate in Fig. 5 is caused by the internal kink mode as the profile of the radial plasma displacement of the instability exhibits a rigid-body displacement inside the $q = 1$ mode rational surface in Fig. 7 (a). Figure 7 (a) also shows that the helical displacement has the similar profile as the eigen-function of the internal-kink mode, implying that the helical core is a saturated state of the growth of an $(m, n) = (1, 1)$ internal-kink instability. In the low $q_{\rm min}$ regime, the profile of the eigen function of the instability is significantly different from that of the internal-kink mode as shown in Fig. 7 (b). The displacement is large near the magnetic axis, implying that the instability is the quasi-interchange mode [32, 33]. A stationary state established by a nonlinear saturation of the quasi-interchange instability is expected to have the helical displacement strongly peaked at the magnetic axis shown in Fig. 7 (b), resulting in the advected deformation of the magnetic flux surfaces around the axis at $q_{\rm min} = 0.8$ in Figs. 2 and 3. The quasi-interchange modes are observed in a wide range of (κ, δ) parameter space as shown by the shoulder at a $q_{\rm min}$ of around 0.8 in Fig. 8. It is remarked that we suitably rescale the eigenfunction to compare its shape with that of helical displacement in Fig. 7, because the amplitude of the eigenfunction obtained from linear stability numerical calculation is arbitrary.

As well as the radial displacement ξ_r, the poloidal component of the plasma displacement ξ_θ suggests that the instabilities at $q_{\rm min} \approx 1$ and 0.8 are significantly different. Figure 9 (a) shows that the poloidal displacement ξ_θ has a peak with negative sign at $q = 1$ rational surface where the radial displacement ξ_r has a sharp drop, while the amplitude of ξ_θ in the core region is small compared to the peak. These are typical features of the eigen function of the internal-kink mode. Figure 9 (b) shows that the plasma displacement (ξ_r, ξ_θ) for $q_{\rm min} = 0.80$ is similar to that for $q_{\rm min} = 1.01$ at $q = 1$ rational surface. In the core region, by contrast, both ξ_r and ξ_θ are large, and the amplitude of ξ_θ near the magnetic axis is comparable with that of the peak at $q = 1$ rational surface at $\rho \approx 0.35$. This large amplitude of the displacement (ξ_r, ξ_θ) near the magnetic axis also implies that the instability at a $q_{\rm min}$ of around 0.8 is the quasi-interchange mode. As shown in Fig. 6, the transition from the internal-kink mode to the quasi-interchange mode is continuous, and thus the plasma

displacement of the quasi-interchange mode in Fig. 9 (b) partially includes the feature of internal-kink mode.

As we discussed above, the displacement δ_H of a helical equilibrium state is related to the linear growth rate of an $(m, n) = (1, 1)$ instability for the corresponding axisymmetric equilibrium. Here, we investigate this relation in detail. Figure 10 shows the helical displacement δ_H as a function of the linear growth rate γ. The curve is drawn as an implicit function of $q_{\rm min}$, and the value of $q_{\rm min}$ is indicated by some arrows in the frame. Each of the loops presented starts at the origin in the δ_H versus γ plane in the counter clockwise sense in which the value of $q_{\rm min}$ is decreasing along the path followed before returning to the origin at low enough $q_{\rm min}$. Each curve exhibits a loop and a sharp peak corresponding to the internal-kink and quasi-interchange driven helical cores, respectively, except for the circular cross section that has only a loop. The loop extending to the top-right corner of the frame represents the internal-kink driven helical-core at $q_{\rm min} \approx 1$. The helical displacement is almost proportional to the linear growth rate, implying that the helical core is a nonlinearly saturated state of the internal-kink mode. With increasing the elongation and triangularity, both the linear growth rate and the excited helical displacement are enhanced. There is another peak of the helical displacement. This sharp peak appearing in the top-left corner represents the quasi-interchange driven helical-core at $q_{\rm min} \approx 0.8$. The displacement is large in the finite γ regime, but its dependence on the linear growth rate is not clear. This is perhaps because this type of helical-core is a nonlinearly saturated state of the quasi-interchange mode that causes the local advection of the magnetic axis.

V. INFLUENCE OF MAGNETIC SHEAR AND BETA

Here, we present that a weak magnetic shear is relevant for the onset of quasi-interchange driven helical cores in the low $q_{\rm min}$ regime, $q_{\rm min} \approx 0.8$. Although we have two $q = 1$ rational surfaces when $q_{\rm min}$ is less than unity as shown in Fig. 1, the helical displacement is large within the inner $q = 1$ surface. One of the reason is that the global magnetic shear $\hat{s} = \frac{\rho}{q}\frac{dq}{d\rho}$ is smaller at the inner rational surface than the outer one. The absolute value of the magnetic shear decreases with lowering $q_{\rm min}$ in Fig. 1, and thus the large helical displacement in the low $q_{\rm min}$ regime can be linked to the weak magnetic shear at the inner $q = 1$ rational surface. In order to clarify this link, we change the magnetic shear at the inner rational surface with

keeping $q_{\rm min}$. The magnetic shear is changed by modifying the value of q at the magnetic axis q_0 and by changing the radial location of the minimum of safety factor $\rho_{\rm qmin}$, while $q(\rho_{\rm qmin}) = q_{\rm min} = 0.8$, $q(\rho = \rho_1 = 0.4) = 1$, and $q(\rho = 1) = 1.5$ are kept as shown in Fig. 11. Figure 12 shows the helical displacement δ_H as a function of the magnetic shear at the inner $q = 1$ rational surface $\hat{s}(\rho = \rho_1)$ with keeping $q_{\rm min} = 0.8$. The helical displacement increases as the absolute value of the magnetic shear $|\hat{s}|$ decreases for both the $\rho_{\rm qmin}$ change and q_0 change cases. Thus, the quasi-interchange driven helical-core at low $q_{\rm min}$ in Fig. 4 is caused by the weak magnetic shear $|\hat{s}| \ll 1$.

Finally, we demonstrate that the magnitude of the quasi-interchange driven helical-core is enhanced with increasing the plasma β. Since the quasi-interchange mode is a pressure-driven instability, the resulting helical displacement due to this instability is expected to be increased with β. Figure 13 shows the helical displacement δ_H as a function of the averaged toroidal beta for the q-profile with $q_{\rm min} = 0.8$, $q_0 = 1.025$ and $\rho_{\rm qmin} = 0.75$ shown in Fig. 11 (b). For $(\kappa, \delta) = (1.2, 0)$, the helical displacement vanishes at $\beta = 0$, and is very small at low-β ($\beta = 0.5\%$), then the displacement increases with increasing β at $\beta > 0.5\%$, consistent with the linear growth rate of the quasi-interchange mode [32]. For $(\kappa, \delta) = (1.6, 0.344)$, the helical displacement increases with increasing β, while the helical displacement is finite at $\beta = 0$. This helical core at $\beta = 0$ is not quasi-interchange driven but internal-kink driven as shown by magnetic surfaces. Figure 14 shows magnetic flux surfaces for $(\kappa, \delta) = (1.6, 0.344)$. A rigid-body displacement in the core region at $\beta = 0$ implies that this helical core is due to an internal-kink mode, while the local advection of the axis region at $\beta = 3\%$ suggests that this helical core is caused by a quasi-interchange mode. Thus, the quasi-interchange driven helical-core is formed as β increases. It is remarked that the shape of magnetic surfaces of the quasi-interchange driven helical core partially includes the feature of internal-kink modes, because the transition from the internal-kink mode to the quasi-interchange mode is continuous as shown in Fig. 6.

VI. SUMMARY

We have investigated equilibrium states with a helical core in weakly reversed magnetic shear tokamaks by means of three-dimensional MHD equilibrium calculations and a linear stability analysis of the corresponding axisymmetric equilibrium. Our $q_{\rm min}$ scan, where $q_{\rm min}$

is the minimum value of safety factor, revealed that helical cores are of two types. The first type appears at a $q_{\min}$ of around unity and is characterized by a rigid-body displacement in the core region. This type of helical-core is commonly observed in our previous work. The other appears at a $q_{\min}$ of about 0.8 and is characterized by a local advection of the plasma at the magnetic axis.

In order to understand the formation mechanism of these two different helical cores we carried out a linear stability analysis of the corresponding axisymmetric equilibrium that has the same q and pressure profiles as the helical equilibrium state. We have found that the helical core appearing at a $q_{\min}$ of around unity is caused by an $(m, n) = (1, 1)$ internal-kink mode, resulting in a rigid-body radial displacement in the core region on a poloidal cross-section. The radial profile of the displacement of the helical core is almost constant inside the $q = 1$ rational surface, which is similar to the eigen function of the internal kink mode. On the other hand, the helical core appearing at a $q_{\min}$ of about 0.8 is caused by an $(m, n) = (1, 1)$ quasi-interchange mode, leading to the displacement only near the magnetic axis. The radial profile of the displacement is sharply peaked at the magnetic axis, that is similar to the profile of the eigen function of the quasi-interchange mode. The appearance of the quasi-interchange driven helical-core in the low $q_{\min}$ regime is related to the weak magnetic shear at the inner $q = 1$ rational surface, and its magnitude is enhanced as β increases. Hence, the weak magnetic shear is the key player in the formation of the quasi-interchange helical state rather than the low $q_{\min}$.

Acknowledgments

This work was supported by the Japanese Ministry of Education, Culture, Sports, Science and Technology, Grant No. 18K03583. Calculations are carried out on JFRS-1 of IFERC-CSC at QST.

Data availability statement

The data that support the findings of this study are available upon reasonable request from the authors.

---

[1] I. T. Chapman, D. Brunetti, P. Buratti, W. A. Cooper, J. P. Graves, J. R. Harrison, J. Holgate, S. Jardin, S. A. Sabbagh, K. Tritz, the MAST and NSTX Teams and EFDA-JET Contributors, Nucl. Fusion **54**, 083007 (2014).

[2] E. Joffrin, F. Crisanti, R. Felton, X. Litaudon, D. Mazon, D. Moreau, L. Zabeo, R. Albanese, M. Ariola, D. Alves, O. Barana, V. Basiuk, et.al., Plasma Phys. Control. Fusion **45**, A367 (2003).

[3] C. Gormezano, A. Becoulet, P. Buratti, et al, Plasma Phys. Control. Fusion 46 B435 (2004).

[4] E. Strumberger, S. Gunter, P. Merkel, E. Schwarz and C. Tichmann, Nucl. Fusion **50** 025008 (2010)

[5] A. Ishizawa, D. Urano, Y. Nakamura, S. Maeyama, and T.-H. Watanabe, Phys. Rev. Lett. **123**, 025003 (2019).

[6] A. Weller, A. D. Cheetham, A. W. Edwards, R. D. Gill, A. Gondhalekar, R. S. Granetz, J. Snipes, and J. A. Wesson, Phys. Rev. Lett. **59**, 2303 (1987).

[7] I.T. Chapman, M.-D. Hua, S.D. Pinches, R.J. Akers, A.R. Field, J.P. Graves, R.J. Hastie, C.A. Michael and the MAST Team, Nucl. Fusion **50**, 045007 (2010).

[8] M. Cianciosa, A. Wingen, S. P. Hirshman, S. K. Seal, E. A. Unterberg, R. S. Wilcox, P. Piovesan, L. Lao and F. Turco, Nucl. Fusion 57 076015 (2017).

[9] T. Bando, G. Matsunaga, M. Takechi, A. Isayama, N. Oyama, S. Inoue, M. Yoshida and T. Wakatsuki, Plasma Phys. Control. Fusion **61** 115014 (2019).

[10] Marshall N. Rosenbluth, R. Y. Dagazian and P. H. Rutherford, Physics of Fluids 16, 1894 (1973).

[11] W. A. Cooper, J. P. Graves, A. Pochelon, O. Sauter, and L. Villard, Phys. Rev. Lett. **105**, 035003 (2010).

[12] W. A. Cooper, J. P. Graves and O. Sauter, Plasma Phys. Control. Fusion 53, 024002 (2011).

[13] W. A. Cooper, J. P. Graves, O. Sauter, I. T. Chapman, M. Gobbin, L. Marrelli, P. Martin, I. Predebon and D. Terranova, Plasma Phys. Control. Fusion 53, 074008 (2011).

[14] W. A. Cooper, J. P. Graves and O. Sauter, Nucl. Fusion 51, 072002 (2011).

[15] W. A. Cooper, J. P. Graves, O. Sauter, J. Rossel, M. Albergante, S. Coda, B. P. Duval, B. Labit, A. Pochelon, H. Reimerdes and the TCV team, Plasma Phys. Control. Fusion 53, 124005 (2011).

[16] A. Wingen, R. S. Wilcox, S. K. Seal, E. A. Unterberg, M. R. Cianciosa, L. F. Delgado-Aparicio, S. P. Hirshman and L. L. Lao, Nucl. Fusion **58** 036004 (2018).

[17] Y. Nakamura, A. Ishizawa, Y. Ishida, Physics of Plasmas, **27**, 092509 (2020)
[18] W. A. Cooper, D. Brunetti, B. P. Duval, J. M. Faustin, J. P. Graves, A. Kleiner, H. Patten, D. Pfefferl, L. Porte, M. Raghunathan, H. Reimerdes, O. Sauter, and T. M. Tran, Physics of Plasmas **23**, 040701 (2016).
[19] M. N. Bussac, R. Pellat, D. Edery, and J. L. Soule, Phys. Rev. Lett. 35, 1638 (1975).
[20] J. A. Wesson, Plasma Phys. Control. Fusion **28** 243 (1986).
[21] R. J. Hastie and T. C. Hender, B. A. Carreras, L. A. Charlton, and J. A. Holmes, Phys. Fluids **30** 1756 (1987).
[22] A. Wingen, R. S. Wilcox, L. F. Delgado-Aparicio, R. Granetz, S. Houshmandyar, S. Shiraiwa, M. R. Cianciosa, and S. K. Seal, Phys. Plasmas **26**, 022501 (2019).
[23] W. Park, D.A. Monticello, R.B. White and S.C. Jardin, Nucl. Fusion 20, 1181 (1980).
[24] D. Brunetti, J.P. Graves, W.A. Cooper and D. Terranova, Nucl. Fusion **54** 064017 (2014).
[25] J. P. Graves, C. Angioni, R. V. Budny, R. J. Buttery, S. Coda, L-G. Eriksson, C. G. Gimblett, T. P. Goodman, R. J. Hastie, M. A. Henderson, H. R. Koslowski, M. J. Mantsinen, An. Martynov, M-L. Mayoral, A. Muck, M. F. F. Nave, O. Sauter, E. Westerhof and JETEFDA Contributors, Plasma Phys. Control. Fusion **47** B121 (2005).
[26] J. P. Graves, D. Zullino, D. Brunetti, S. Lanthaler and C. Wahlberg, Plasma Phys. Control. Fusion **61**, 104003 (2019)
[27] S. P. Hirshman and J. C. Whitson, Phys. Fluids **26**, 3553 (1983).
[28] S. P. Hirshman, W. I. van Rij and P. Merkel, Comput. Phys. Commun. **43**, 143 (1986).
[29] S. P. Hirshman and H. K. Meier, Phys. Fluids **28** 1387 (1985).
[30] M. Azumi, G. Kurita, T. Matsuura, T. Takeda, Y. Tanaka, T. Tsunematsu, "A fluid model numerical code system for tokamak fusion research", Proc. 4th Int. Symp. on Comput. Methods Applied Sci. Engineering, Paris (North-Holland, Amsterdam, 1980) p.335.
[31] N. Aiba, S. Tokuda, M. Furukawa, P. B. Snyder, M. S. Chu, Comput. Phys. Commun. **180**, 1282 (2009).
[32] F. L. Waelbroeck, and R. D. Hazeltine, Physics of Fluids **31**, 1217 (1988).
[33] F. L. Waelbroeck, Physics of Fluids **B 1**, 499 (1989).
[34] J. Freidberg, *Ideal MHD*, Cambridge (2014).

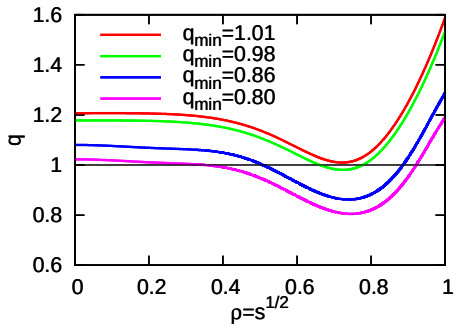

FIG. 1: Profiles of safety factor, where $\rho = \sqrt{s}$ is the normalized minor radius.

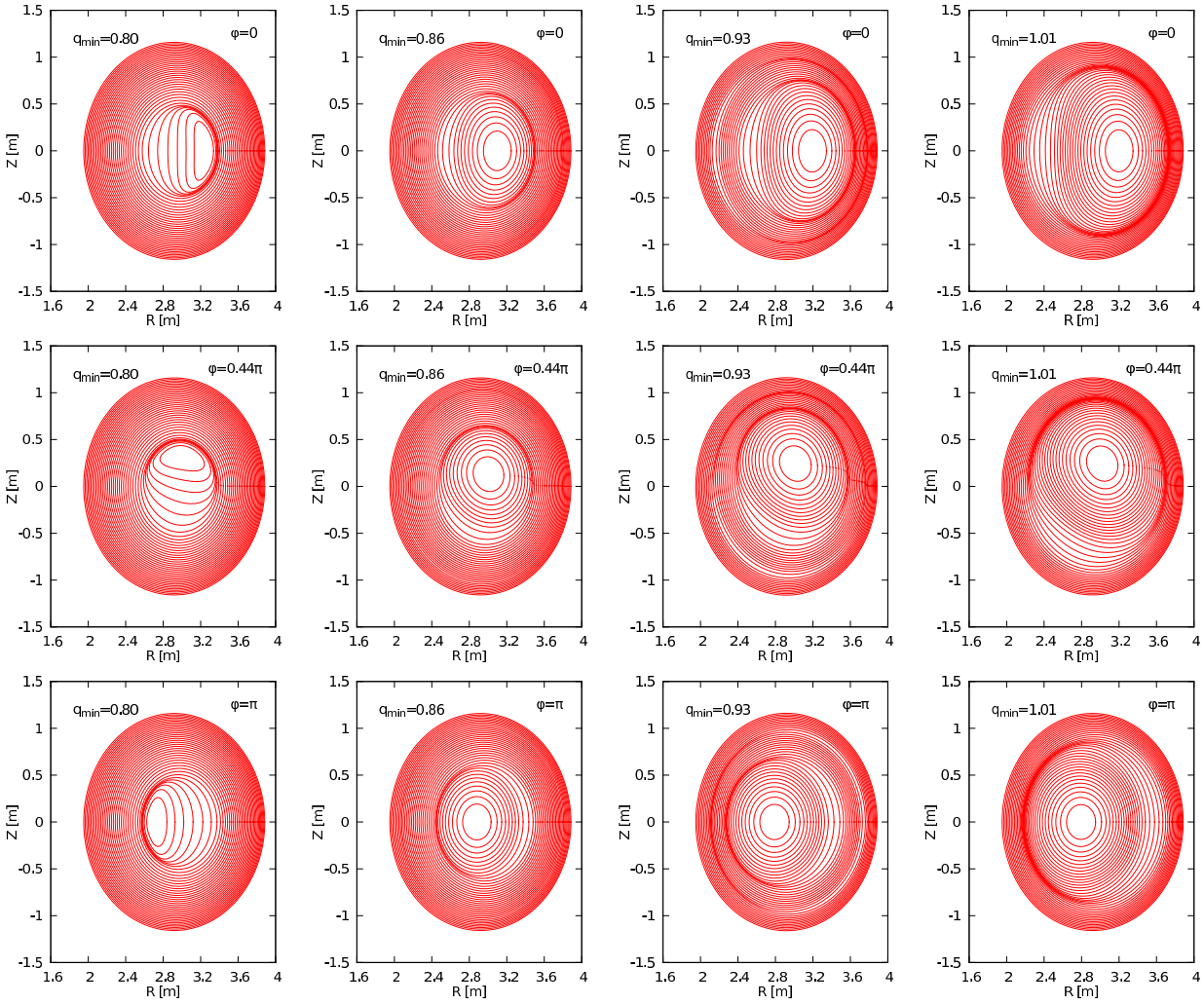

FIG. 2: Magnetic surfaces at a toroidal angle $\phi = 0$, 0.44π and π for elongation $\kappa = 1.2$, triangularity $\delta = 0$, and $\beta = 3\%$, showing a rigid-body shift in the core region like an internal kink mode at $q_{\min} \geq 0.86$ and a locally advected shift at the magnetic axis suggesting a quasi-interchange mode at $q_{\min} = 0.80$.

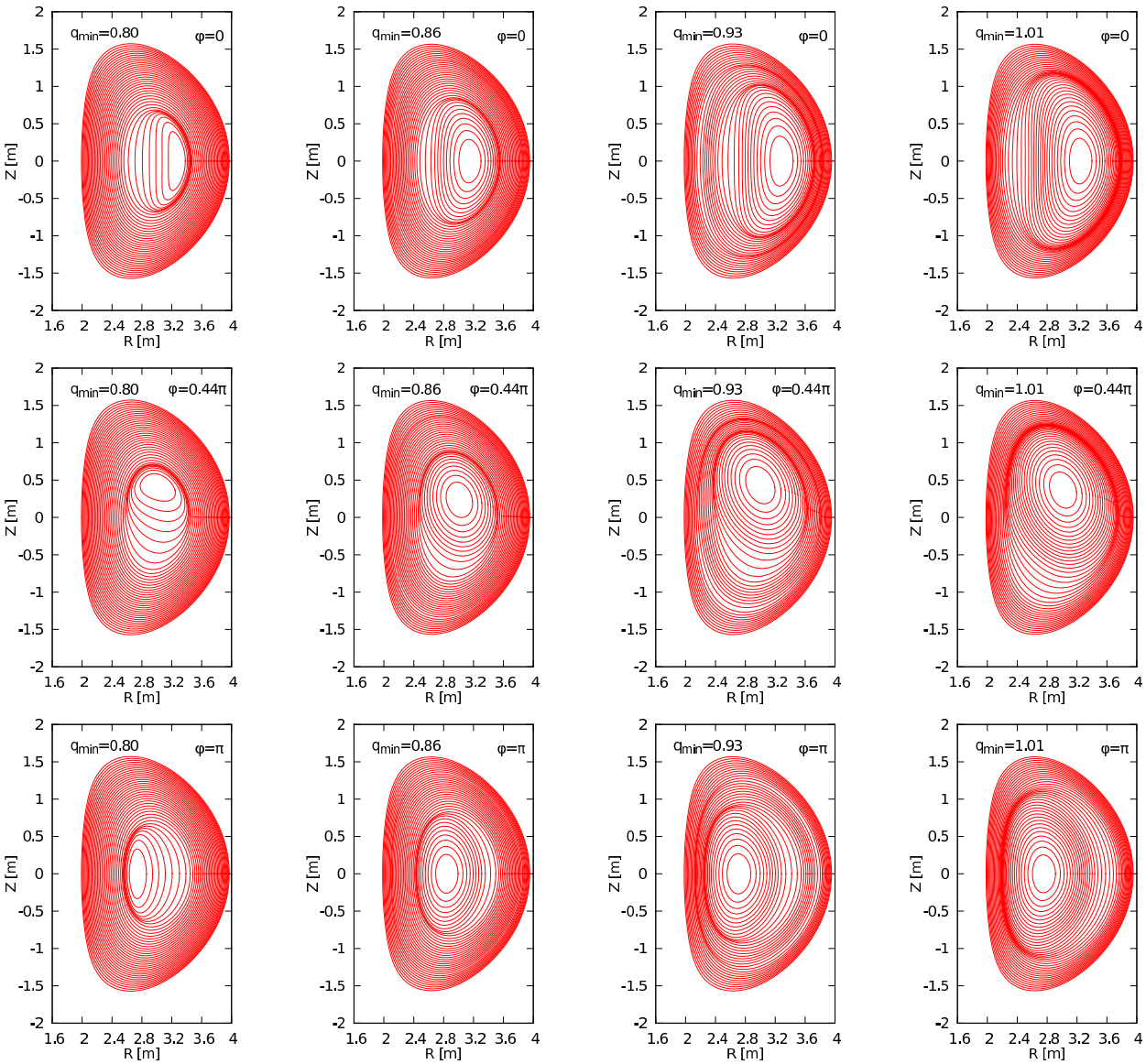

FIG. 3: Magnetic surfaces at a toroidal angle $\phi = 0, 0.44\pi$ and π for elongation $\kappa = 1.6$, triangularity $\delta = 0.344$, and $\beta = 3\%$, showing a rigid-body shift in the core region like an internal kink mode at $q_{\min} \geq 0.86$ and a locally advected shift at the magnetic axis suggesting a quasi-interchange mode at $q_{\min} = 0.80$.

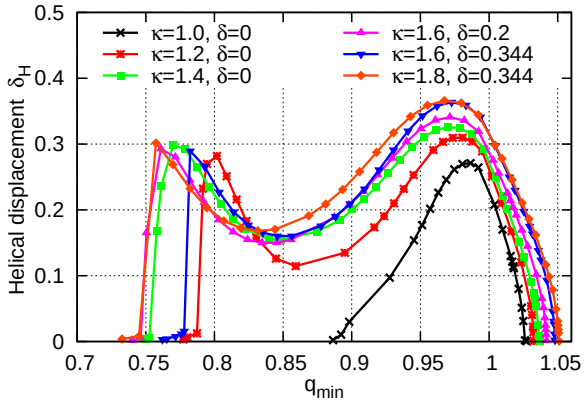

FIG. 4: Helical displacement δ_H as a function of the minimum value of the safety factor $q_{\min}$ for several sets of elongation κ and triangularity δ, and $\beta = 3\%$.

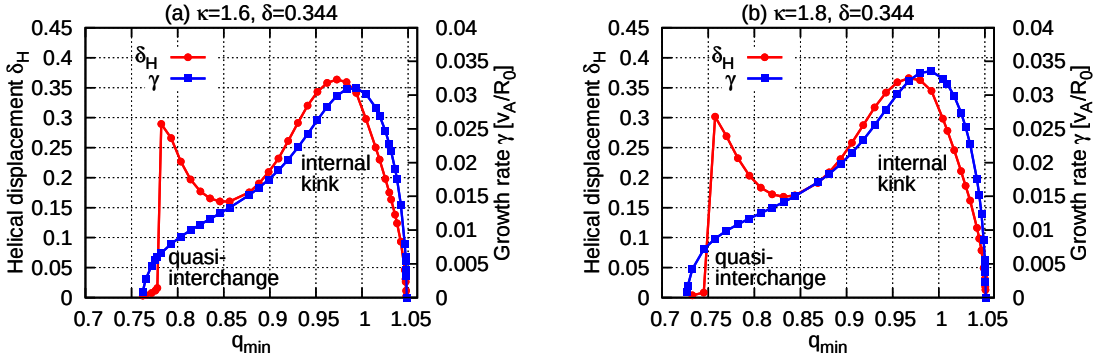

FIG. 5: Helical displacement δ_H and linear growth rate γ of an $(m, n) = (1, 1)$ mode as a function of $q_{\min}$ at $\beta = 3\%$ for (a) $\kappa = 1.6$ and $\delta = 0.344$ and (b) $\kappa = 1.8$ and $\delta = 0.344$.

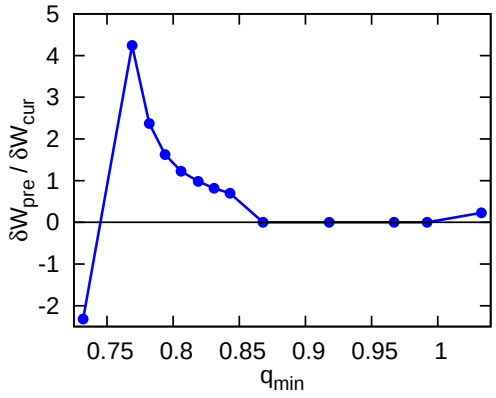

FIG. 6: The ratio of the pressure driven term $\delta W_{\rm pre}$ to the current driven term $\delta W_{\rm cur}$ in the ideal MHD energy principle as a function of $q_{\min}$ for $(\kappa, \delta) = (1.8, 0.344)$ at $\beta = 3\%$.

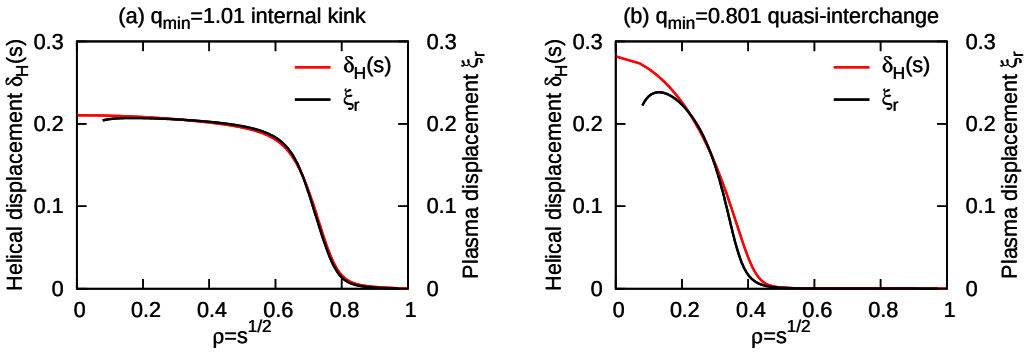

FIG. 7: Helical displacement δ_H and the radial displacement of the $(m, n) = (1, 1)$ Fourier component of the eigenfunction ξ_r for $\kappa = 1.2$ and $\delta = 0$ at $\beta = 3\%$ in the case (a) $q_{\min} = 1.01$ and (b) $q_{\min} = 0.801$, where $\rho = \sqrt{s}$ is the normalized minor radius.

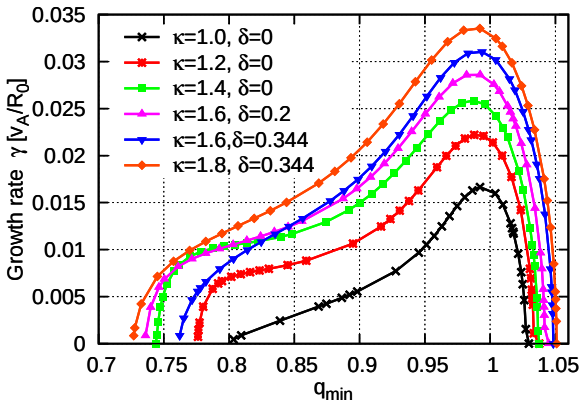

FIG. 8: Linear growth rate γ as a function of $q_{\min}$ for $\beta = 3\%$.

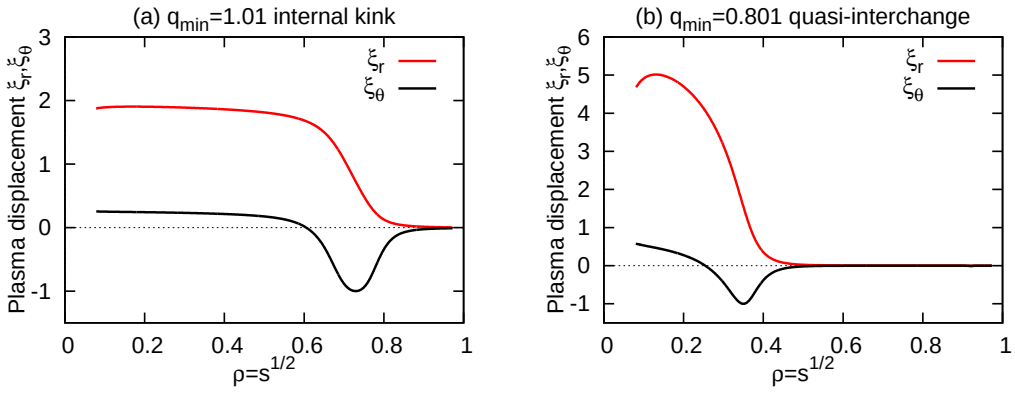

FIG. 9: Profiles of the radial and poloidal components of the plasma displacement (ξ_r, ξ_θ) for $(m, n) = (1, 1)$ Fourier component of the eigenfunction at $\kappa = 1.2$, $\delta = 0$ and $\beta = 3\%$ (a) $q_{\min} = 1.01$ and (b) $q_{\min} = 0.80$.

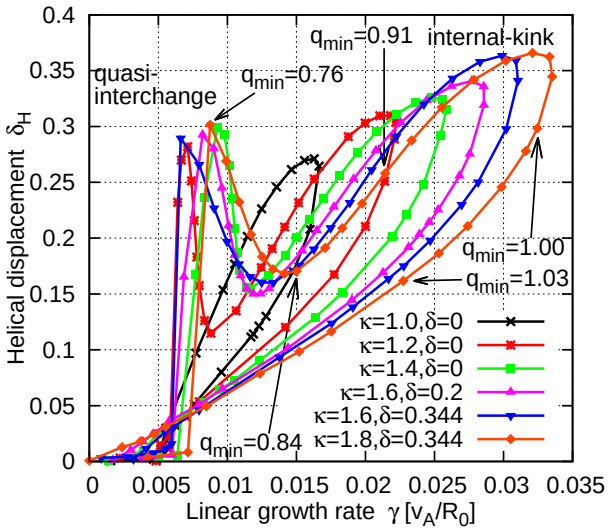

FIG. 10: Helical displacement δ_H as a function of the linear growth rate γ for $\beta = 3\%$. Some values of $q_{\min}$ on the curve for $(\kappa, \delta) = (1.8, 0.344)$ are pointed by arrows.

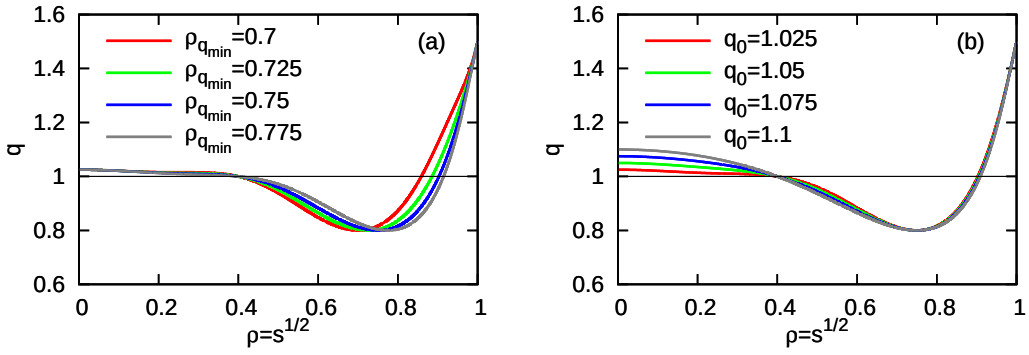

FIG. 11: Profiles of safety factor with $q_{\rm min} = 0.8$ for various values of magnetic shear at the inner $q = 1$ rational surface at $\rho = 0.4$ by changing (a) the radius of the minimum of safety factor $\rho_{\rm qmin}$ and (b) the value of safety factor at the magnetic axis q_0.

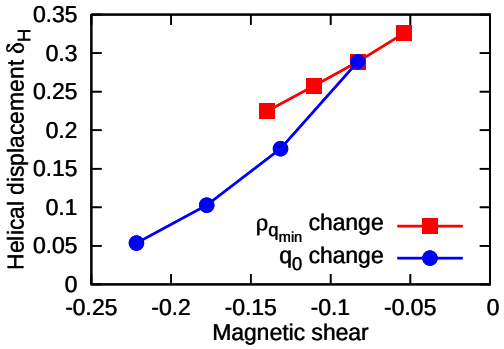

FIG. 12: Helical displacement δ_H as a function of magnetic shear $\hat{s}$ at the inner $q = 1$ rational surface for $q_{\rm min} = 0.8$.

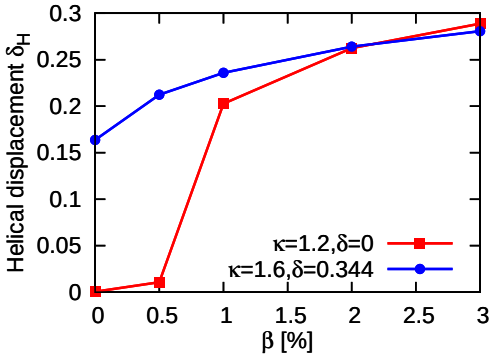

FIG. 13: Helical displacement δ_H as a function of β for $q_{\rm min} = 0.8$.

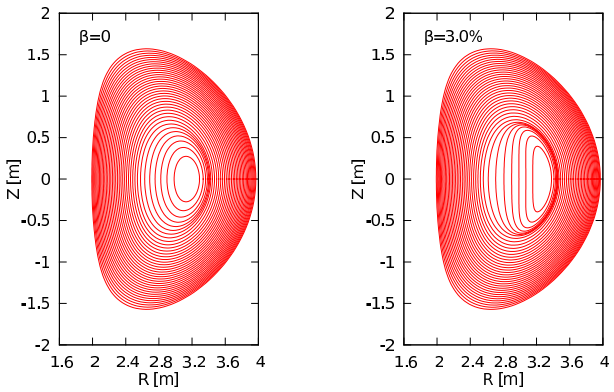

FIG. 14: Magnetic surfaces for $(\kappa, \delta) = (1.6, 0.344)$ showing an internal-kink driven helical-core at $\beta = 0\%$ and a quasi-interchange driven helical-core at $\beta = 3\%$.